



**HAL**  
open science

# Modular Self-Assembling Dendrimer Nanosystems for Magnetic Resonance And Multimodality Imaging of Tumors

Ling Ding, Zhenbin Lyu, Teodora-adriana Perles-Barbacaru, Adela Ya-ting Huang, Baoping Lian, Yifan Jiang, Tom Roussel, Christina Galanakou, Suzanne Giorgio, Chai-lin Kao, et al.

► **To cite this version:**

Ling Ding, Zhenbin Lyu, Teodora-adriana Perles-Barbacaru, Adela Ya-ting Huang, Baoping Lian, et al.. Modular Self-Assembling Dendrimer Nanosystems for Magnetic Resonance And Multimodality Imaging of Tumors. *Advanced Materials*, 2023, 10.1002/adma.202308262 . hal-04315766v2

**HAL Id: hal-04315766**

**<https://hal.science/hal-04315766v2>**

Submitted on 13 Dec 2023

**HAL** is a multi-disciplinary open access archive for the deposit and dissemination of scientific research documents, whether they are published or not. The documents may come from teaching and research institutions in France or abroad, or from public or private research centers.

L'archive ouverte pluridisciplinaire **HAL**, est destinée au dépôt et à la diffusion de documents scientifiques de niveau recherche, publiés ou non, émanant des établissements d'enseignement et de recherche français ou étrangers, des laboratoires publics ou privés.



Distributed under a Creative Commons Attribution 4.0 International License

# Modular Self-Assembling Dendrimer Nanosystems for Magnetic Resonance and Multimodality Imaging of Tumors

Ling Ding, Zhenbin Lyu, Teodora-Adriana Perles-Barbacaru, Adela Ya-Ting Huang, Baoping Lian, Yifan Jiang, Tom Roussel, Christina Galanakou, Suzanne Giorgio, Chai-Lin Kao, Xiaoxuan Liu, Juan Iovanna, Monique Bernard, Angèle Viola, and Ling Peng\*

Bioimaging is a powerful tool for diagnosing tumors but remains limited in terms of sensitivity and specificity. Nanotechnology-based imaging probes able to accommodate abundant imaging units with different imaging modalities are particularly promising for overcoming these limitations. In addition, the nanosized imaging agents can specifically increase the contrast of tumors by exploiting the enhanced permeability and retention effect. A proof-of-concept study is performed on pancreatic cancer to demonstrate the use of modular amphiphilic dendrimer-based nanoprobe for magnetic resonance (MR) imaging (MRI) or MR/near-infrared fluorescence (NIRF) multimodality imaging. Specifically, the self-assembly of an amphiphilic dendrimer bearing multiple  $Gd^{3+}$  units at its terminals, generates a nanomicellar agent exhibiting favorable relaxivity for MRI with a good safety profile. MRI reveals an up to two-fold higher contrast enhancement in tumors than in normal muscle. Encapsulating the NIRF dye within the core of the nanoprobe yields an MR/NIRF bimodal imaging agent for tumor detection that is efficient both for MRI, at  $Gd^{3+}$  concentrations 1/10 the standard clinical dose, and for NIRF imaging, allowing over two-fold stronger fluorescence intensities. These self-assembling dendrimer nanosystems thus constitute effective probes for MRI and MR/NIRF multimodality imaging, offering a promising nanotechnology platform for elaborating multimodality imaging probes in biomedical applications.

## 1. Introduction

Cancer is one of the leading causes of death worldwide and remains a difficult disease to treat. Early and accurate diagnosis positively influences the effective management of cancer. It provides the opportunity to intervene during the early stages of disease, leading to more effective treatment, increased survival rates, and in some cases even a complete cure. In this context, bioimaging plays an important role in cancer diagnosis, by allowing non-invasive tumor detection and staging, as well as an assessment of treatment efficacy.<sup>[1,2]</sup> However, bioimaging remains limited in terms of sensitivity, specificity, and accuracy, as well as toxicity associated with certain imaging agents.


The application of nanotechnology to bioimaging offers the potential to overcome some or all of these limitations.<sup>[3,4]</sup> Specifically, nanosized agents can carry an abundance of imaging reporters, thereby significantly improving imaging sensitivity. In addition, nanotechnology allows the combining of different imaging modalities within

L. Ding, Z. Lyu, A. Y.-T. Huang, Y. Jiang, T. Roussel, C. Galanakou, S. Giorgio, L. Peng  
Aix Marseille University  
CNRS  
Centre Interdisciplinaire de Nanoscience de Marseille (UMR 7325)  
Equipe Labellisée Ligue Contre le Cancer  
Marseille 13288, France  
E-mail: ling.peng@univ-amu.fr

L. Ding, T.-A. Perles-Barbacaru, M. Bernard, A. Viola  
Aix Marseille University  
CNRS  
Centre de Résonance Magnétique Biologique et Médicale (CRMBM)  
UMR 7339, Marseille 13385, France

A. Y.-T. Huang, C.-L. Kao  
Department of Medicinal and Applied Chemistry  
Drug Development and Value Creation Research Center  
Kaohsiung Medical University  
100 Shih-Chuan 1st Road, Kaohsiung 80708, Taiwan

B. Lian, X. Liu  
State Key Laboratory of Natural Medicines and Jiangsu Key Laboratory of Drug Discovery for Metabolic Diseases  
Center of Drug Discovery  
Center of Advanced Pharmaceuticals and Biomaterials  
China Pharmaceutical University  
Nanjing 210009, P. R. China

 The ORCID identification number(s) for the author(s) of this article can be found under <https://doi.org/10.1002/adma.202308262>

© 2023 The Authors. Advanced Materials published by Wiley-VCH GmbH. This is an open access article under the terms of the Creative Commons Attribution License, which permits use, distribution and reproduction in any medium, provided the original work is properly cited.

DOI: 10.1002/adma.202308262

the same nanosystem. This enables multimodality imaging that provides more precise and complete information compared to that obtained using single-modality imaging. Furthermore, nanosized agents may home in on and accumulate within tumors by way of the “enhanced permeability and retention (EPR)” effect.<sup>[5–10]</sup> This effect is based on the leaky vasculature and dysfunctional lymphatic drainage found in the tumor microenvironment. This enables the accumulation of the nanosized agents within the tumor, thereby improving imaging sensitivity and specificity for cancer diagnosis. Clinical studies have confirmed the existence of the EPR effect within certain human tumors, however, the relevance of the EPR phenomenon occurring for all nanoparticles and in all patients and tumors is now debated.<sup>[11–13]</sup> Recent studies show that tumor vascular permeability represents a dynamic phenomenon that can promote nanoparticle delivery.<sup>[14]</sup> In addition, some inorganic nanoparticles can even directly produce gaps in the tumor vessel wall thereby generating the vascular leakiness required to produce the EPR effect.<sup>[15]</sup> Also, tumor targeting based on transcytosis<sup>[16,17]</sup> and in situ tumor-generated extracellular vesicle-mediated delivery<sup>[18,19]</sup> have been proposed for effective penetration of nanoparticles deep within the tumor. Together, these various mechanisms of nanoparticle access to tumors highlight the potential of nanotechnology-based tumor-specific targeting.

Self-assembly is one powerful strategy for constructing modular and specific nanosystems with relative synthetic ease.<sup>[20,21]</sup> We have recently established innovative supramolecular amphiphilic dendrimer nanosystems for tumor imaging,<sup>[22–24]</sup> exploiting the multivalent cooperativity of dendrimers, the self-assembly of amphiphiles and nanotechnology-based tumor targeting.<sup>[25,26]</sup> We specifically developed the imaging nanoprobe for effective tumor imaging using single photon emission computed tomography and positron emission tomography (PET).<sup>[22–24]</sup> In particular, one of these nanoprobe successfully detected tumors that are otherwise undetectable using 2-fluorodeoxyglucose, the clinical standard for PET imaging of tumors.<sup>[22]</sup> This exceptional imaging success can be ascribed to the abundance of imaging units conjugated to the dendrimer terminals at the nanoprobe surface, as well as to the EPR-mediated tumor accumulation and targeting.

Motivated by these promising results, we wanted to further expand on the potential applications for self-assembling dendrimer nanosystems by integrating together different imaging agents for multimodality imaging. One frequently used imaging modality is MRI, which provides anatomic, functional, and metabolic information with good spatial resolution and unlimited tissue penetration.<sup>[27,28]</sup> While this is particularly beneficial for the detection of deep-seated and small tumors, the MRI signal is not specific and the contrast between tumor and surrounding tissue often needs improving using contrast agents.<sup>[29]</sup>

Nanotechnology-based contrast agents offer the unique advantage of benefiting from passive tumor targeting and deep tumor penetration. This results in high specificity and sensitivity for tumor tissue and minimal biodistribution to healthy tissues, hence improving MRI contrast while minimizing general toxicity.<sup>[3,30]</sup> Another imaging modality is fluorescence imaging which offers high sensitivity but is limited by tissue penetration depth. The use of near-infrared fluorescence (NIRF) probes permits real-time imaging and allows the evaluation of tumor margins for intra-operative imaging-guided surgery.<sup>[31–33]</sup> Multimodality imaging combining MRI and NIRF imaging is expected to harness the advantages of both imaging modalities while overcoming their individual shortcomings, thereby allowing highly sensitive and specific imaging of tumors through the retrieval of complementary information.<sup>[34]</sup>

Specifically in this study, we aimed to create modular self-assembling dendrimer nanosystems for tumor detection using MRI alone or multimodality imaging combining MRI and NIRF imaging (**Figure 1A**). Considering that most clinical MRI contrast agents are based on paramagnetic gadolinium ( $Gd^{3+}$ ), which requires high coordination with water,<sup>[35]</sup> we conceived the dendrimer nanomicellar system **Gd-1@** comprising the amphiphilic dendrimer **Gd-1** with  $Gd^{3+}$  contrast units at its hydrophilic terminals for MRI (**Figure 1B**). The aim was to construct a nanosystem offering both the multivalent characteristics of dendrimers and easy access to water toward  $Gd^{3+}$  at the dendrimer surface. To prevent toxicity and stability issues from free  $Gd^{3+}$ , the macrocyclic chelator 1,4,7,10-tetraazacyclododecane-1,4,7,10-tetraacetic acid (DOTA) was conjugated at the dendrimer terminals and coordinated with  $Gd^{3+}$  to form a Gd-DOTA complex with high thermodynamic and kinetic stability.<sup>[29,35]</sup>

The unique radiating dendritic structure of the amphiphilic dendrimer **Gd-1** was expected to allow, once self-assembled, the loading of hydrophobic agents in the large void space formed within the inner core of the **Gd-1@** nanomicelles, as with the loading of drugs for cancer treatment. Considering that NIRF probes are often hydrophobic and insoluble in water, we therefore conceived the dendrimer nanoprobe **DiR/Gd-1@** formed from the amphiphilic dendrimer **Gd-1** (**Figure 1B**) with the hydrophobic NIRF dye DiR loaded within the core of the nanoparticle for bimodality MR/NIRF imaging (**Figure 1**). The  $Gd^{3+}$  contrast units at the hydrophilic dendrimer terminals for MRI and the hydrophobic NIRF dye DiR encapsulated within the core for NIRF imaging, ensured the segregation in space of the imaging reporters and prevented their eventual interference during multimodality imaging.

We report here the construction and use of these modular self-assembling nanosystems formed from **Gd-1** for MRI and MR/NIRF bimodality imaging of pancreatic cancer as a proof-of-concept study. Pancreatic cancer is a deadly cancer, difficult to diagnose early on and with, as of yet, no efficacious treatment.<sup>[36–38]</sup> The most effective treatment for pancreatic cancer is surgical ablation. However, for most patients, this is no longer an option due to the lack of effective early detection making their diagnosis of now advanced and metastatic forms too late to allow effective surgical ablation.<sup>[39]</sup> Therefore, the early detection of pancreatic cancer with a non-invasive imaging modality is of paramount importance. We demonstrate in this study that the nanoprobe **Gd-1@** enabled cancer detection using MRI with signal enhancement in

J. Iovanna  
Centre de Recherche en Cancérologie de Marseille  
INSERM U1068  
CNRS  
UMR 7258  
Institut Paoli-Calmettes  
Aix Marseille Université  
Marseille 13273, France

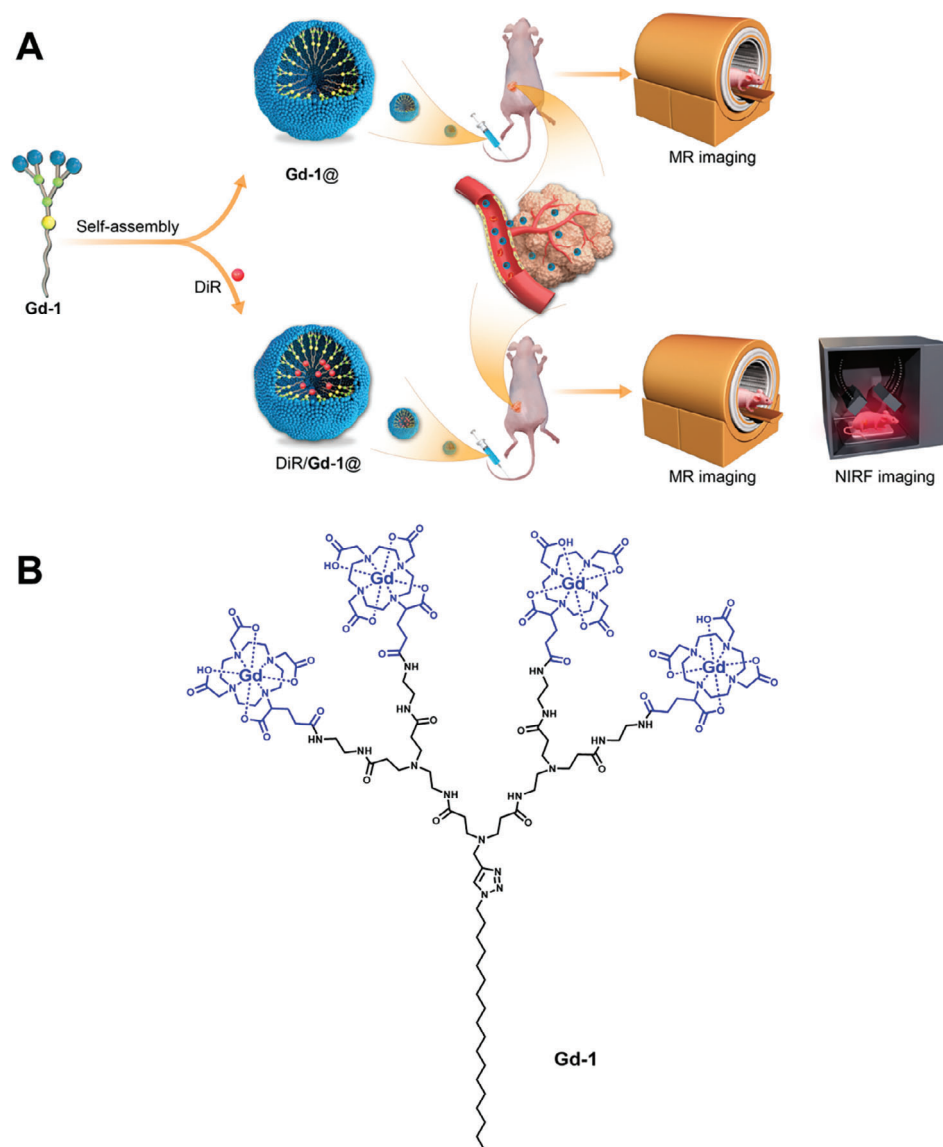


**Figure 1.** Self-assembling dendrimer nanosystems for imaging tumors using magnetic resonance and multimodal imaging techniques. A) Schematic illustration of self-assembling dendrimer nanosystems **Gd-1@** and **DiR/Gd-1@** as imaging agents, respectively, for MRI and MR/NIRF bimodality imaging of tumor via EPR effect-based passive tumor targeting. B) Chemical structure of the amphiphilic dendrimer **Gd-1**.

tumors at a Gd dose tenfold lower than the conventional dose of the clinical standard Gd-DOTA. In addition, the use of the probe **DiR/Gd-1@** enabled the sensitive detection of pancreatic cancer by MR/NIRF bimodality imaging. These modular supramolecular dendrimer nanosystems offer a new platform for constructing crude dendrimer agents that hold great promise for both MRI and MR/NIRF multimodality imaging.

## 2. Results and Discussion

### 2.1. Synthesis of Dendrimer **Gd-1** and its Self-Assembly into Nanomicelles

The Gd-bearing dendrimer **Gd-1** was synthesized by chelating the dendrimer **1** with  $\text{Gd}^{3+}$  (Figure 2A). Specifically, **1** was pre-

pared according to the protocol previously established in our group.<sup>[23]</sup> Then  $\text{GdCl}_3$  was added in three portions to the aqueous solution of **1** at 24 °C, with the pH of the reaction mixture maintained at 6.5 to ensure optimal acidic conditions for effective chelation between **1** and  $\text{Gd}^{3+}$ . To address the thermodynamically challenging chelation between  $\text{Gd}^{3+}$  and the DOTA cage, the reaction mixture was heated to 50 °C for 24 h under argon to achieve complete chelation. The resulting crude dendrimer **Gd-1** was purified using dialysis to remove the excess free  $\text{Gd}^{3+}$ , giving the final product **Gd-1** as a white solid with a yield of up to 92% after lyophilization.

Mass spectroscopic analysis confirmed the successful synthesis of **Gd-1**, showing clear-cut peaks for the double-charged (**Gd-1-2H**)<sup>2-</sup> and triple-charged species (**Gd-1-3H**)<sup>3-</sup> corresponding to the expected molecular weight of **Gd-1** (Figure 2B).

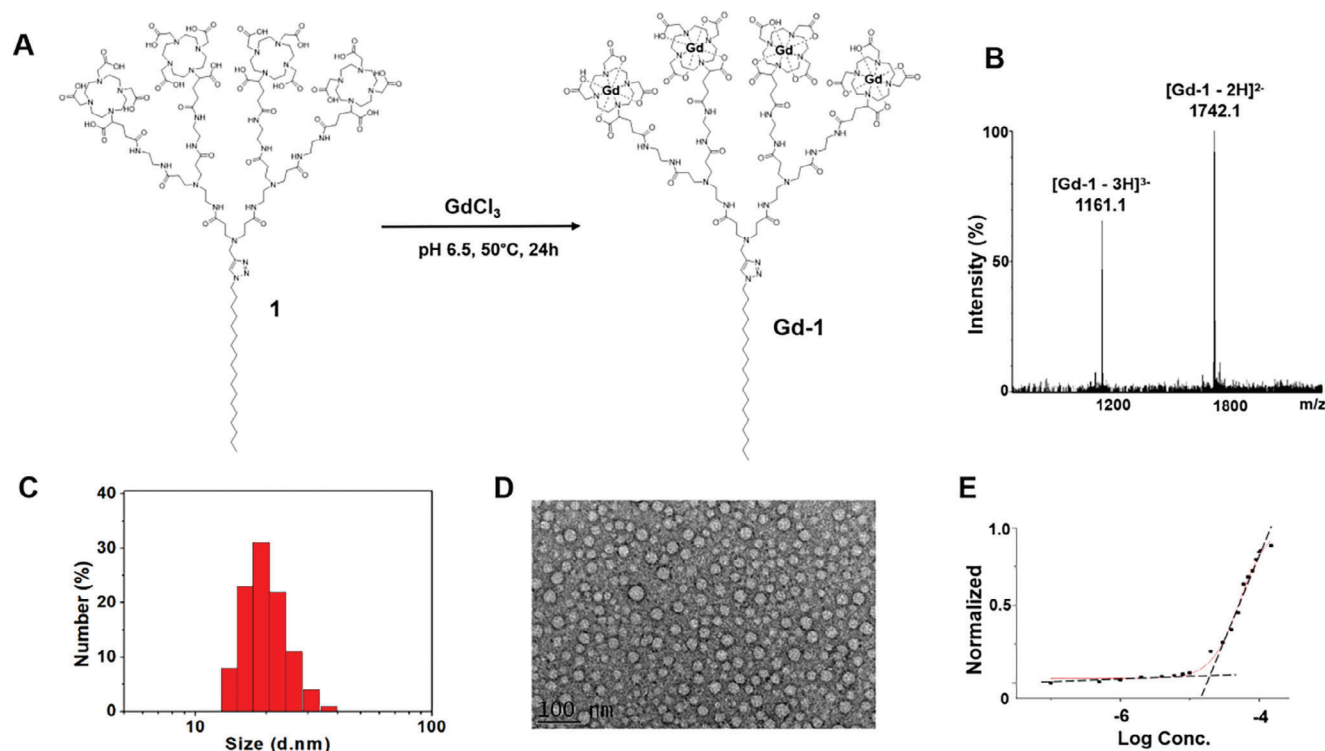


**Figure 2.** Synthesis of Gd-1 and its self-assembly into nanomicellar particles Gd-1@. A) Synthesis scheme and reaction conditions for preparing Gd-1. B) Mass spectroscopic analysis of Gd-1. C) Dynamic light scattering analysis of Gd-1@ nanoparticles formed spontaneously by Gd-1 in H<sub>2</sub>O. D) Transmission electron microscope image of Gd-1@ nanoparticles. E) Evaluation of CMC of Gd-1 using fluorescent spectroscopic analysis with Nile red.

Additionally, inductively coupled plasma mass spectrometry (ICP-MS) was performed to quantify the content of Gd in Gd-1. A Gd content of 17% obtained from ICP-MS agreed with the theoretical value for the chemical structure of Gd-1, further supporting the successful chelation of Gd<sup>3+</sup> in all four DOTA cages.

Gd-1 spontaneously self-assembled in water by virtue of its amphiphilic nature. We first studied the self-assembled nanoparticles Gd-1@ using dynamic light scattering (DLS) analysis. The DLS results revealed the formation of small nanoparticles of Gd-1@ with a size of  $\approx 23 \pm 1$  nm, a typical size for nanomicelles (Figure 2C). We further examined Gd-1@ using transmission electron microscopy (TEM), and the obtained TEM data confirmed the formation of small, uniform, and spherical nanomicelles of Gd-1@ with average dimensions of  $\approx 21 \pm 4$  nm (Figure 2D; Figure S1, Supporting Information), similar to the estimation obtained using DLS (Figure 2C). It is to note that the optimal size best-permitting nanoparticles to exploit the EPR effect for passive tumor targeting and deep tumor penetration is in the range of 12–30 nm. If too small, the nanoparticles will be rapidly removed via renal clearance but will generate steric hindrance for deep tumor penetration if too big.<sup>[40–42]</sup> Thus, Gd-1@ having a size of  $\approx 20$  is particularly interesting for its use in nanotechnology-based bioimaging.

The critical micelle concentration (CMC) of Gd-1 was then assessed using a fluorescence spectroscopic assay with Nile red. The obtained CMC value of  $27 \pm 3$  mM (Figure 2E) strongly supports the formation of Gd-1@ nanomicelles. The amphiphilic dendrimer Gd-1 was thus shown to readily and spontaneously self-assemble into small nanomicelles in water.

## 2.2. Advantageous Relaxivity with Enhanced MRI Signals at High Magnetic Field Strength

To explore the potential of Gd-1@ as a contrast agent for MRI, it was important to study its ability to decrease the longitudinal  $T_1$  and transverse  $T_2$  relaxation time constants of water media.  $T_1$  shortening by the paramagnetic ion Gd<sup>3+</sup> results in a signal increase visualized on  $T_1$ -weighted MRI as hyperintensities (bright signals), whereas  $T_2$  shortening is associated with signal loss on  $T_2$ -weighted MRI.<sup>[29]</sup> Relaxivity reflects the efficiency of the contrast agent to increase the longitudinal and transverse relaxation rates ( $1/T_1$  and  $1/T_2$ ) of water.<sup>[29,35]</sup> Although Gd-based contrast agents have relatively high longitudinal  $r_1$  relaxivity and generally provide good contrast characteristics at low magnetic field strength, they are often less effective at high magnetic field strengths.<sup>[28,35,43]</sup> Today however, the demand for MRI scanners operating at high magnetic field strengths ( $\geq 7$  T) is increasing because of the better signal-to-noise ratio compared to those functioning at lower magnetic field strengths. Considering the tendency of the tissue contrast in  $T_1$ -weighted images to decrease with increasing magnetic field strength, we wished to develop efficient contrast agents with good relaxivity at high magnetic field strength to improve imaging quality.

We therefore first assessed the relaxivity of Gd-1@ in water using an MRI scanner operating at a magnetic field strength of 11.75 T, using the leading contrast agent gadoterate meglumine (Gd-DOTA, also commercially referred to as Dotarem) as the reference control. By linearly fitting the  $T_1$  relaxation rate ( $1/T_1$ ) against the Gd<sup>3+</sup> concentration (Figure 3A), we obtained an  $r_1$

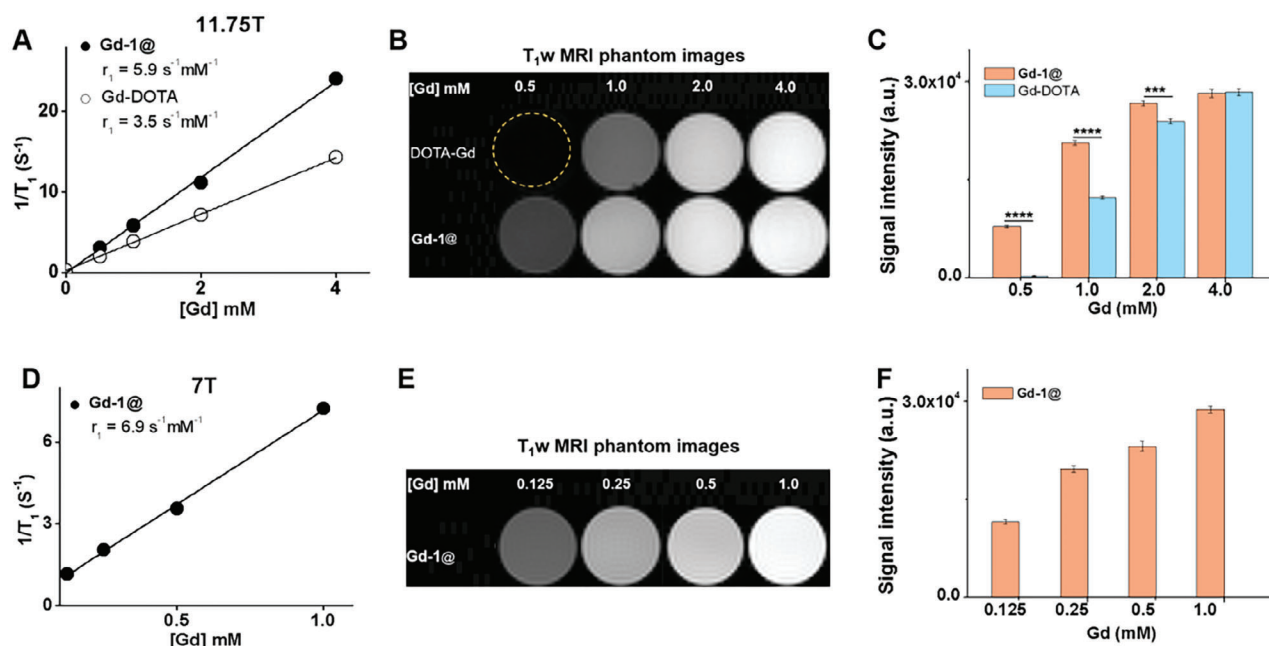


**Figure 3.** Favorable relaxivity of the Gd-1@ nanoparticles and enhanced MRI signals at 11.75 T and 7 T. A) Longitudinal relaxation rate  $1/T_1$  of Gd-1@ as a function of Gd concentration in water at 11.75 T and 20 °C. The slope of the linear fit corresponds to relaxivity. The clinical contrast agent Gd-DOTA was used as the reference control. B)  $T_1$ -weighted MRI ( $T_1$ w MRI) phantom images and C) MRI signal intensity of Gd-1@ and Gd-DOTA solutions obtained at 11.75 T with different Gd concentrations. Data are presented as mean  $\pm$  SD. The statistical significance was calculated using a two-tailed Student's *t*-test ( $n = 3$ , \*\*\*\* $P < 0.0001$ , \*\*\*\*\* $P < 0.00001$ ). D) Longitudinal relaxation rate  $1/T_1$  of Gd-1@ as a function of Gd concentration in water at 7 T and 20 °C. The slope of the linear fit corresponds to the relaxivity. E)  $T_1$ w MRI phantom images and F) MRI signal intensity of Gd-1@ solutions obtained at 7 T with different Gd concentrations. The coefficients of determination in (A) and (D) are  $R^2 > 0.99$ .

value of  $5.9 \text{ s}^{-1} \text{ mM}^{-1}$  (95% confidence interval 5.4–6.4) for Gd-1@, almost twofold higher than that for Gd-DOTA ( $3.5 \text{ s}^{-1} \text{ mM}^{-1}$ , 95% confidence interval 3.4–3.6). The enhanced  $r_1$  relaxivity of Gd-1@ compared to Gd-DOTA can be ascribed not only to its macromolecular and nanosized structure but also to its strongly hydrophilic and multivalent surface allowing increased interaction of  $\text{Gd}^{3+}$  ions with water molecules. This constitutes a valuable asset for Gd-1@ when used as a  $T_1$  contrast agent in MRI.

We next performed phantom studies and acquired  $T_1$ -weighted MRI of Gd-1@ and Gd-DOTA at different Gd concentrations (Figure 3B). Both Gd-1@ and Gd-DOTA showed an increasing signal intensity with increasing Gd concentrations on  $T_1$ -weighted MRI. However, the higher relaxivity of Gd-1@ provided brighter MRI signals compared to those from Gd-DOTA at the same Gd concentration (Figure 3B,C). In particular, at the low Gd concentration of 0.5 mM, at which the Gd-DOTA solution yielded an almost negligible  $T_1$ -weighted MRI signal, the signal generated with Gd-1@ was over 30-fold stronger (Figure 3C, Table S1, Supporting Information). These results highlight that even at very low Gd concentrations, Gd-1@ meets the need for an efficient contrast agent for  $T_1$ -weighted MRI at ultra-high magnetic field strength.

We also examined the relaxivity of Gd-1@ using an MRI scanner operating at a magnetic field strength of 7 T, which is used routinely in preclinical MRI studies but recently also in clinical settings. The  $r_1$  value obtained for Gd-1@ at 7 T was  $6.9 \text{ s}^{-1} \text{ mM}^{-1}$ , with a 95% confidence interval of 6.1–7.7 (Figure 3D), which was only slightly higher than that obtained at 11.75 T ( $5.9 \text{ s}^{-1} \text{ mM}^{-1}$ ). Similarly,  $T_1$ -weighted MRI of Gd-1@ showed enhanced inten-

sities at increasing Gd concentrations (Figure 3E,F). Altogether, these data provide evidence supporting the ability of Gd-1@ nanoparticles to retain high  $r_1$  relaxivity for  $T_1$ -weighted MRI at high magnetic field strengths. The resulting increased magnetic polarization and consequently improved signal is advantageous for detecting smaller lesions.

### 2.3. Excellent Safety Profile of Gd-1@ Nanoparticles

For all bioimaging applications, the safety of the imaging agents is an important consideration. Some Gd-based contrast agents have been reported to cause severe side effects such as nephrogenic systemic fibrosis in patients with renal failure.<sup>[44,45]</sup> It was therefore necessary to assess the safety profile of Gd-1@ prior to in vivo bioimaging studies.

We first examined the metabolic cytotoxicity of Gd-1@ on various cells using the PrestoBlue cell viability assay. At Gd concentrations up to 2000  $\mu\text{M}$ , Gd-1@ exhibited no notable cytotoxicity on different cell lines including human kidney cells (HEK293), Madin–Darby canine kidney cells (MDCK), alpha mouse liver 12 cells (AML12), and murine fibroblast cells (L929) (Figure 4A). These results support the high potential of Gd-1@ in biomedical studies.

We also evaluated the effect of Gd-1@ on cell membrane integrity using the lactate dehydrogenase (LDH) assay for which LDH release signals plasma membrane damage. The lack of obvious LDH release for any of the tested cell lines at Gd

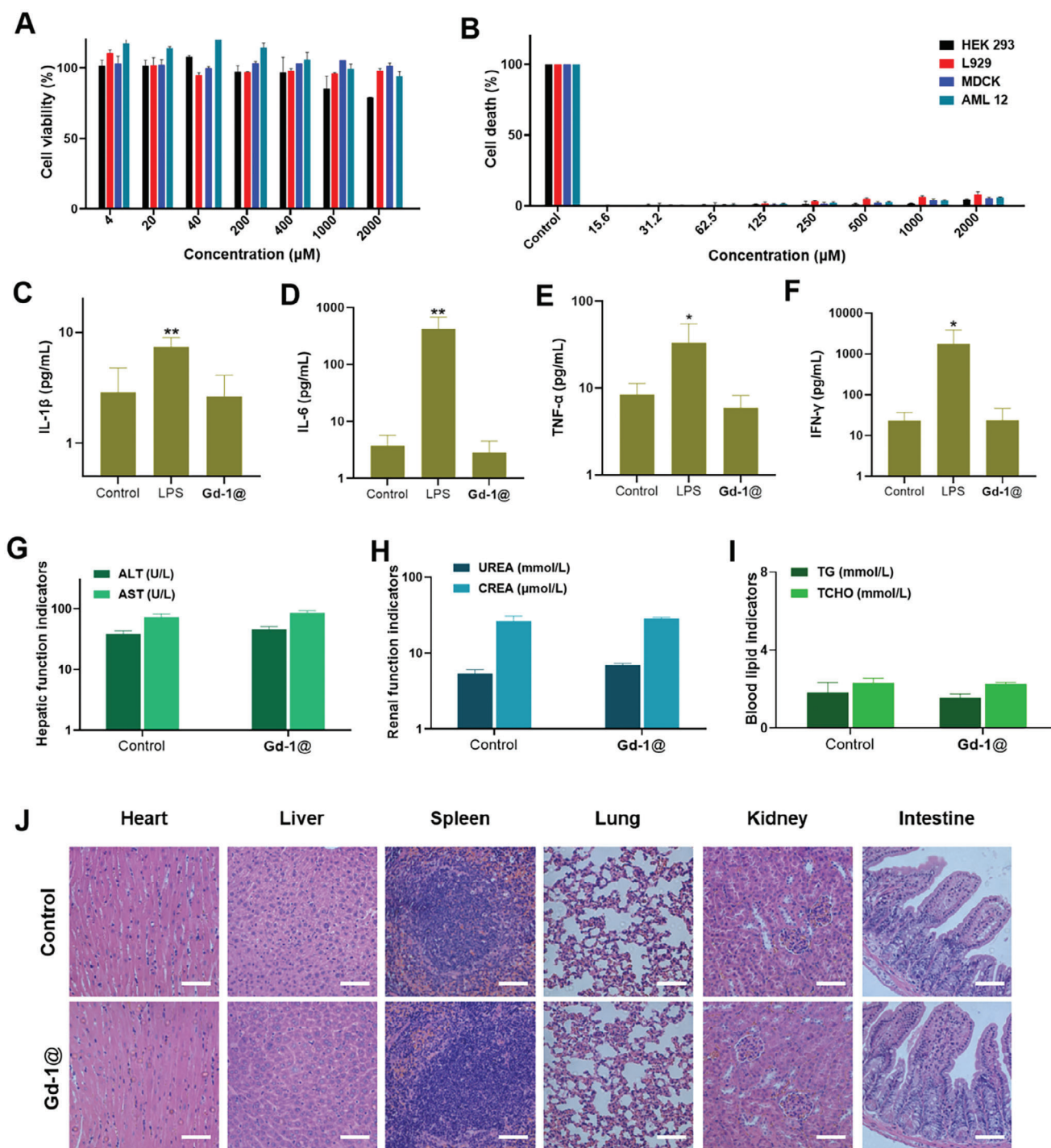


**Figure 4.** Safety evaluation of Gd-1@. A) Toxicity evaluation of Gd-1@ on HEK293, MDCK, AML12, and L929 cells in a Gd<sup>3+</sup> concentration range of 4 to 2000  $\mu\text{M}$  at 48 h post-treatment using the PrestoBlue assay. B) Evaluation of membrane damage by Gd-1@ on HEK293, MDCK, AML12, and L929 cells in a Gd<sup>3+</sup> concentration range of 15.6 to 2000  $\mu\text{M}$  using LDH assay. Lysis buffer provided in the commercial LDH assay kit was used as a positive control (Control). C–J) In vivo toxicity evaluation of Gd-1@ in healthy mice ( $n = 4$  for each group of mice). Quantification of the major inflammatory cytokines in serum C) IL-1 $\beta$ , D) IL-6, E) TNF- $\alpha$ , and F) INF- $\gamma$ . Data are presented as mean  $\pm$  SD ( $n = 4$ ). The statistical significance was analyzed by one-way ANOVA with a Tukey's multiple comparison test (ns not significant, \* $P < 0.05$ , \*\* $P < 0.01$ ). Assessment of liver and kidney function and of blood lipids by quantifying the levels of biomarkers G) alanine aminotransferase (ALT) and aspartate aminotransferase (AST), H) urea and creatinine, I) triglycerides and total cholesterol in serum. J) Histological analysis of tissues from major organs using hematoxylin and eosin staining. Mice received either Gd-1@ (22.0 mg  $\text{k}^{-1}$  g, iv injection) or normal saline (control, iv injection). Scale bar, 200  $\mu\text{m}$ .

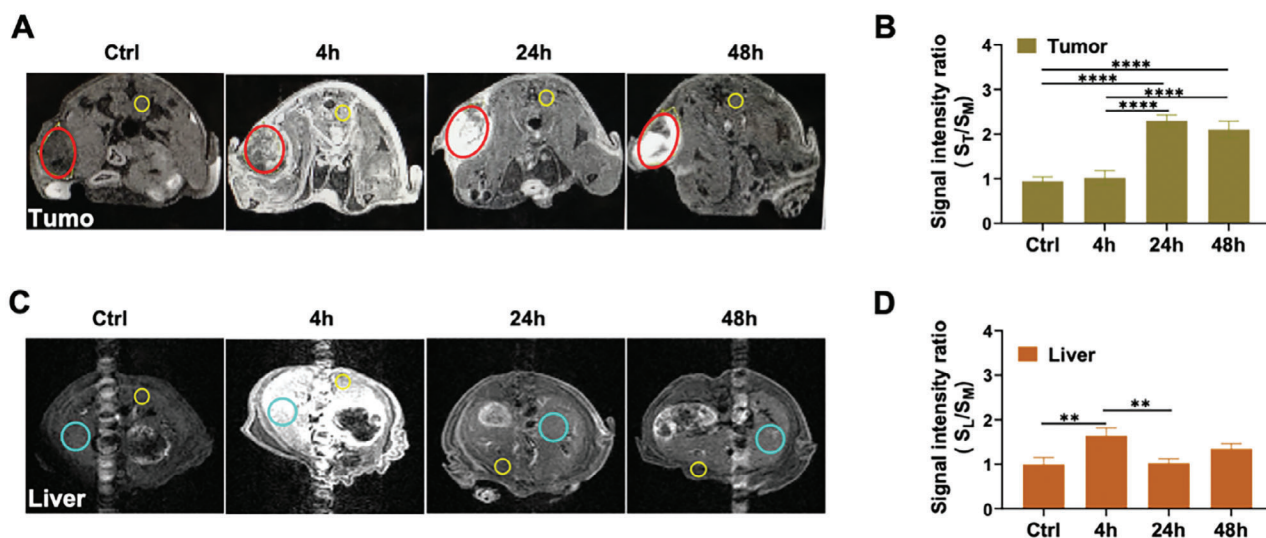


**Figure 5.** In vivo MRI of tumor and liver using Gd-1@ at ultra-high magnetic field (11.75 T). Transverse MRI of mice bearing L-IPC pancreatic tumor before (control, CTRL) and 4, 24, and 48 h after iv injection of Gd-1 (dose of 0.05 mmol Gd kg<sup>-1</sup>), (*n* = 3 for each group of mice). The MR images show uptake of Gd-1@ in A) subcutaneous tumor (red oval) and C) liver (cyan circle) in the same mouse. A flow artifact (produced by the phase encoding) from the aorta is visible in the abdominal MRI (C) but was avoided when drawing the region of interest (ROI) for liver signal analysis. Changes in signal intensity ratios of B) tumor and D) liver after Gd-1@ injection. Paravertebral muscles were used for normalization and highlighted with yellow circles. Data are presented as the mean ± SD (*n* = 3). The statistical significance was calculated using ANOVA with Tukey's multiple comparison test (\*\**P* < 0.01, \*\*\*\**P* < 0.0001).

concentrations ranging from 15.6 to 2000 μM (Figure 4B) demonstrated the biocompatibility of Gd-1@ for further application.

We next assessed inflammatory response to Gd-1@, as well as blood biochemistry and pathology in major organs of healthy mice. While mice in the positive control group treated with lipopolysaccharide (LPS) showed significantly increased levels of the inflammatory factors IL-1β, IL-6, TNF-α, and INF-γ (Figure 4C–F), those treated with Gd-1@ exhibited inflammatory cytokine levels similar to those found in the negative control group of mice treated with normal saline. These results indicate that Gd-1@ induces no inflammatory reactions. Additionally, the liver function indicators alanine aminotransferase (ALT) and aspartate aminotransferase (AST) (Figure 4G), and the kidney function indicators urea and creatinine (Figure 4H), confirmed no functional injury of the liver or kidney. The lack of difference in the levels of the blood lipid markers cholesterol and triglycerides between the Gd-1@ treatment group and the saline control group (Figure 4I) further emphasized the biocompatibility of Gd-1@. Additional histochemical analysis of main organs using hematoxylin and eosin staining revealed that mice treated with Gd-1@ showed normal cell morphology with regularly arranged cells comparable to those found in the control group treated with saline (Figure 4J). This indicates no pathological effect upon treatment with Gd-1@ and, together with the in vitro data above, demonstrates that Gd-1@ has a satisfactory safety profile for further in vivo bioimaging studies.

#### 2.4. In Vivo MRI of Tumors at High Magnetic Field Strength

Motivated by the excellent safety profile and promising relaxivity properties of Gd-1@, we performed in vivo MRI experiments in a tumor xenograft model generated with primary pancreatic can-

cer L-IPC cells from a human patient.<sup>[22,46]</sup> Considering the almost twofold higher relaxivity of Gd-1@ compared with the clinical agent Gd-DOTA at 11.75 T, we injected Gd-1@ at a dose of 0.05 mmol Gd kg<sup>-1</sup>, corresponding to half of the typical clinical dose (0.10 mmol Gd kg<sup>-1</sup>) of Gd-DOTA. We acquired a T<sub>1</sub>-weighted MRI of the tumor (Figure 5A) and the liver (Figure 5C) before and at 4, 24, and 48 h post-injection of Gd-1@ in order to monitor the enhancement of the MRI signals. All these experiments were performed at the ultra-high magnetic field of 11.75 T.

As shown in Figure 5A,C, strong MRI signals were observed throughout the body of the tested mice with intense enhancement in the liver at 4 h post-injection of Gd-1@. However, at 24 and 48 h post-injection, while the MRI signals drastically decreased in the liver and normal tissues (Figure 5C,D), they were significantly enhanced in the tumor (Figure 5A,B). These results indicate the clearance of Gd-1@ from liver and normal tissues and its specific accumulation in tumor that permits the sensitive and specific tumor detection and imaging. We attribute this tumor-specific enrichment of Gd-1@ to the EPR effect of the tumor microenvironment harboring leaky vasculature and dysfunctional lymphatic drainage. This phenomenon allows passive tumor targeting by promoting the accumulation and retention of nanosized imaging agents within the tumor lesion rather than normal tissue, hence enabling effective tumor imaging and detection. It is also to note that pancreatic cancer cells show enhanced macropinocytosis activity<sup>[47,48]</sup> which, alongside the EPR effect, likely contributes toward the significant uptake and accumulation of Gd-1@ within the tumor lesion thus promoting effective and specific tumor imaging.

Importantly, the T<sub>1</sub>-weighted MRI signals in the liver were very weak at 24 and 48 h post-injection, reaching intensity levels similar to those recorded prior to Gd-1@ injection (Figure 5C,D). These data support the rapid clearance of Gd-1@ from the liver



and excretion in urine, thus avoiding any eventual toxicity associated with retention in healthy tissues. We also note that no mice treated with **Gd-1@** showed any abnormal behavior at any point, or any notable weight loss during the experimental period. These results correlate well with those obtained for the safety assay of **Gd-1@** in healthy mice (Figure 4).

## 2.5. Multimodal MR/NIRF Imaging

Encouraged by the excellent results obtained with **Gd-1@** for tumor imaging using MRI, we next constructed the nanoprobe **DiR/Gd-1@** for multimodality MR/NIRF imaging. We did this by encapsulating the NIRF dye DiR within the nanomicelles formed by **Gd-1**, reaching an encapsulation yield of up to 99% using the film-dispersion method.<sup>[49]</sup> The **DiR/Gd-1@** nanoparticles retained the characteristic excitation and emission spectra of DiR in the near-infrared range (Figure 6A), similar to that shown by free DiR dye dissolved in organic solvent (Figure S2, Supporting Information). This fluorescence spectroscopic feature is an important prerequisite for the use of **DiR/Gd-1@** in NIRF imaging.

Remarkably, the **DiR/Gd-1@** nanoparticles were small and uniform in shape, similar to, though slightly smaller (19–20 nm) (Figure 6B; Figure S3, Supporting Information) than, **Gd-1@** (21–23 nm). This difference in size might be ascribed to the hydrophobic DiR loaded within the nanomicellar core, which enabled the assembly of more compact **DiR/Gd-1@** nanoparticles via the enhanced interaction between DiR and the hydrophobic chain in the dendrimer. The resulting smaller nanosize would be expected to be beneficial, by facilitating extravasation and deep penetration into tumor parenchyma, thus enabling more efficient EPR-based accumulation in tumors.<sup>[22,40,49]</sup>

We next investigated whether encapsulation of DiR had an impact on the MRI properties of the Gd/DOTA terminals on the surface of **DiR/Gd-1@**. **DiR/Gd-1@** and **Gd-1@** showed no statistical difference in terms of  $r_1$  relaxivities at 7 T (Figure 6C), respectively  $6.6 \text{ s}^{-1} \text{ mM}^{-1}$  (95% confidence interval, 6.5–6.7) and  $6.9 \text{ s}^{-1} \text{ mM}^{-1}$  (Figure S4A, Supporting Information). Consequently,  $T_1$ -weighted MR images from **DiR/Gd-1@** solutions at different concentrations (Figure 6D) provided similar signal intensities to those of **Gd-1@** solutions (Figure S4B, Supporting Information). These results indicate that encapsulation of DiR has no obvious effect on the access of water protons to **DiR/Gd-1@**, which thus maintains good relaxivity. This can be reasonably explained by the DiR molecules being encapsulated within the interior hydrophobic core and thereby sufficiently segregated in space in relation to the Gd/DOTA entities located on the surface of the **DiR/Gd-1@**.

Importantly, **DiR/Gd-1@** was devoid of any notable toxicity. Indeed, at concentrations up to 1.0 mM, it caused no metabolic cytotoxicity or membrane damage (Figure S5A,B, Supporting Information). The in vivo safety evaluation performed using healthy mice also revealed no alteration of the major blood biochemical markers (alanine transaminase, aspartate transaminase, urea, creatinine, triacylglycerol, and total cholesterol) (Figure S5C–E, Supporting Information), indicating that liver and kidney functioned well with good biocompatibility following administration of **DiR/Gd-1@**. In addition, histological analysis of the main organs showed no pathological changes (Figure S5F, Supporting

Information). The lack of cytotoxic effects and acute toxicity highlights a good and reliable safety profile for **DiR/Gd-1@**, similar to **Gd-1@**.

Encouraged by the excellent safety profile and MRI properties and performance shown by **Gd-1@** at a dose of 0.05 mmol Gd  $\text{kg}^{-1}$  in the above-mentioned MRI studies, we wished to further reduce the Gd dose for the MR/NIRF bimodality imaging. We used **DiR/Gd-1@** at the low dose of 0.025 mmol Gd  $\text{kg}^{-1}$  and an ultra-low dose of 0.010 mmol Gd  $\text{kg}^{-1}$  (Figure 6E), corresponding respectively to 1/4 and 1/10 of the clinically recommended dose (0.10 mmol Gd  $\text{kg}^{-1}$ ). As in the above-mentioned experiments, we used the patient-derived pancreatic cancer L-IPC xenograft model and the clinical contrast agent Gd-DOTA as the control for in vivo MRI studies. Gd-DOTA is a non-specific low molecular weight contrast agent with a short circulation time and a blood half-life of less than 30 min in mice. As expected therefore, we observed no MRI signal enhancement in tumors 30 minutes post-injection when compared with the images acquired prior to injection using the MRI scanner operating at the magnetic field strength of 7 T (Figure 6E, upper panel). These results agree with those reported in the literature and confirm the lack of retention of Gd-DOTA within the tumor lesion and its rapid elimination from the body.<sup>[50]</sup>

In contrast, **DiR/Gd-1@** at doses of 0.010 and 0.025 mmol Gd  $\text{kg}^{-1}$  displayed contrast enhancement at 24 and 48 h post-injection (Figure 6E, middle and lower panels). Notably, at the tumor site, the signal intensity at 24 h was significantly higher than at 48 h post-injection, which can be ascribed to a maximum tumor uptake of **DiR/Gd-1@** at 24 h post-injection and subsequent gradual elimination over time. The MRI sensitivity for tumor detection was quantified as the difference in signal intensity between the tumor and adjacent normal muscle tissues. As shown in Figure 6F, the contrast enhancement at both 24 and 48 h was significant with respect to the pre-injection timepoint. The much-reduced Gd-dose and the longer persistence within the tumor observed with **Gd-1@**, alongside an effective contrast enhancement are particularly advantageous, as they allow for preventing eventual Gd-related toxicity and permitting a longer observation period if necessary (at least 48 h after injection).

At 48 h post-injection, the same mice used for the in vivo MRI experiments were then subjected to NIRF imaging to generate matched sets of dual-modality imaging data. We observed strong fluorescence signals at the tumor sites in mice treated with **DiR/Gd-1@** but no signal at all in the control mice treated with saline or small molecular DiR dye alone (Figure 6G). The results of the NIRF imaging of tumors with **DiR/Gd-1@** concord well with those obtained using MRI. In addition, the NIRF signals in the tumor were two to threefold stronger than those of nearby tissues (Figure 6H). The signal hyperintensities in tumor tissue shown on both MRI and NIRF imaging confirm that **DiR/Gd-1@** is a promising nanoprobe for sensitive and specific MR/NIRF dual-modality tumor imaging.

## 3. Conclusion

In this study, we developed modular dendrimer nanoprobe for MRI and MR/NIRF bimodality imaging, respectively. These

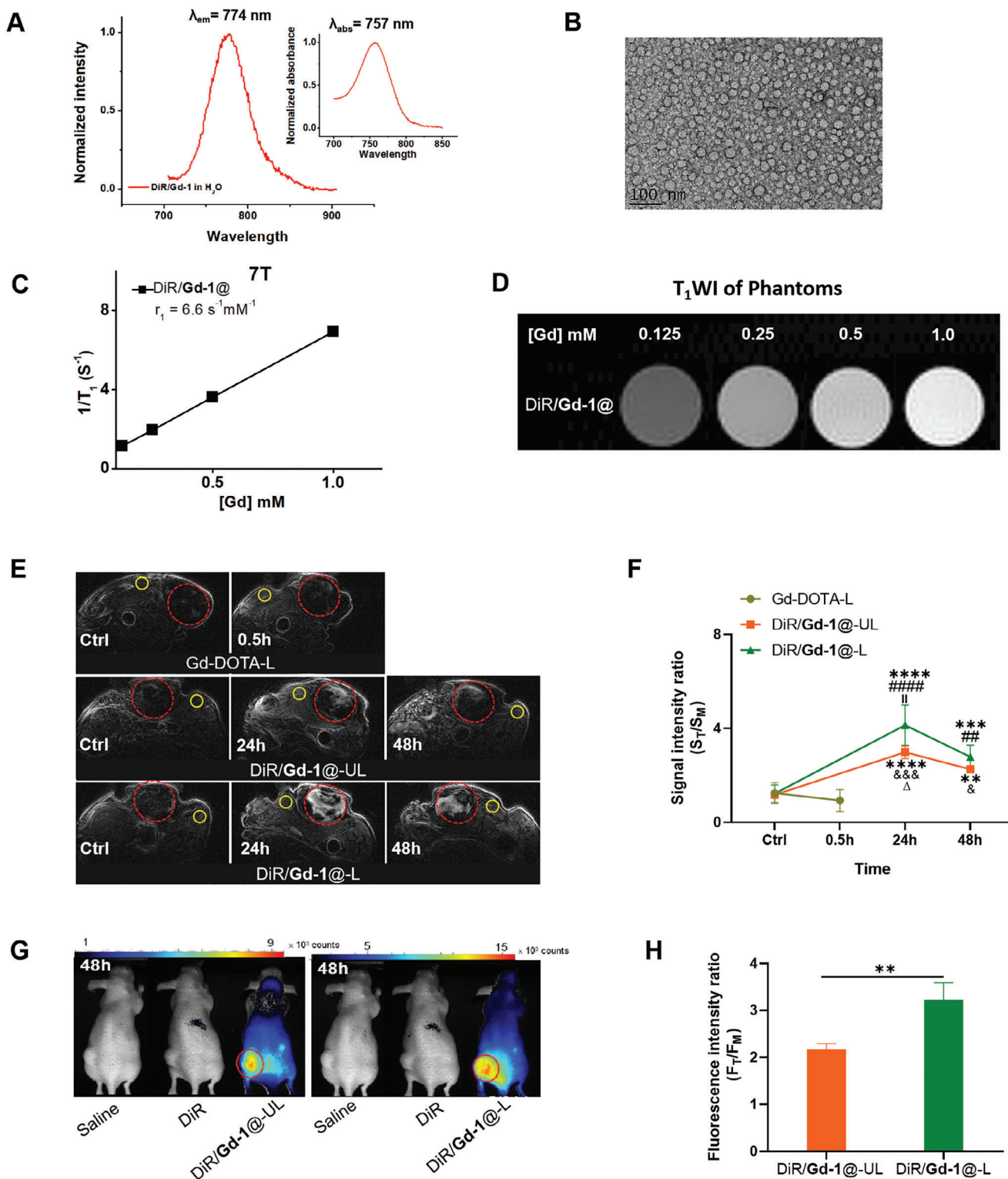


**Figure 6.** DiR/Gd-1@ for MR/NIRF dual imaging of tumor. A) Normalized absorbance and emission spectra of DiR/Gd-1@ in H<sub>2</sub>O. B) Transmission electron microscope imaging of DiR/Gd-1@. C) Longitudinal relaxation rate  $1/T_1$  for DiR/Gd-1@ as a function of Gd concentration. The slope of the linear fit with  $R^2 > 0.99$  corresponds to the relaxivity of the contrast agent in water at 7 T and 20 °C. D)  $T_1$ -weighted MRI of solutions of DiR/Gd-1@ at different Gd concentrations. E–H) Multimodal MR/NIRF imaging of the L-IPC-xenograft mice before (control, ctrl) and after iv injection of DiR/Gd-1@ ( $n = 3$  for each group of mice). E) Transverse  $T_1$ -weighted MRI acquired at 7 T of tumors in L-IPC xenograft mice injected with Gd-DOTA at a low dose (Gd-DOTA-L, 0.025 mmol Gd kg<sup>-1</sup>; upper panel), DiR/Gd-1@ at an ultra-low dose (DiR/Gd-1@-UL, 0.01 mmol Gd kg<sup>-1</sup>, 27 μg DiR/kg; middle panel)

nanoprobe were constructed through self-assembly of the amphiphilic dendrimer **Gd-1**, which is composed of a long hydrophobic alkyl chain and a small hydrophilic poly(amidoamine) dendron bearing four  $Gd^{3+}$  ions chelated within the DOTA rings at the terminals. By virtue of their small nanosize and abundance of multivalent terminals, the nanoprobe **Gd-1@** and **DiR/Gd-1@** showed high levels of accumulation in tumor tissue and higher  $r_1$  relaxivity than the clinical standard Gd-DOTA. This resulted in excellent tumor imaging contrast at low Gd-doses down to 1/10th of the standard clinical dose of Gd-DOTA. Additionally, the **DiR/Gd-1@** probe harbored the NIRF dye DiR within its core for NIRF imaging. The localization of this fluorescence dye at the core meant that it was sufficiently segregated in space away from the Gd/DOTA terminals to avoid any impact on the relaxivity, thereby providing sensitive MR and NIRF imaging of the tumor.

In this proof-of-concept study, the self-assembling dendrimer nanosystems provided not only enhanced imaging contrast for both MRI and NIRF imaging but also effective imaging at much lower Gd doses compared to the clinically used dose. This is an important advantage as it permits the prevention of eventual  $Gd^{3+}$ -related toxicity. The other advantage of **Gd-1@** or **DiR/Gd-1@** in comparison to clinically approved agents is their long half-lives within tumor tissue, likely due to the EPR effect and enhanced macropinocytosis activity found in the tumor microenvironment. This prolonged steady-state concentration within tumor tissue permits high-resolution imaging in cases where a long observation time is required. The capacity to acquire images with increased spatial resolution and contrast also increases the chance of detecting small lesions for early diagnosis. Consequently, the **DiR/Gd-1@** probe shows great promise for use in MRI and MR/NIRF dual imaging and offers the potential for improved imaging efficacy at very low doses for the early detection of pancreatic cancer, an unmet medical need. Further studies dedicated to detailed pharmacokinetic investigation, long-term safety evaluation, and robust validation in different tumor models are required for the translation of these nanosystems into real-life applications.

Since the first MRI study on dendrimer-based contrast agents by Lauterbur in 1994,<sup>[51]</sup> dendrimers have been considered and appreciated as valuable molecular marvels for bioimaging by virtue of their unique precise structure, geometrical symmetry, and cooperative multivalency.<sup>[22,30,52,53]</sup> This study has demonstrated the potential of self-assembling dendrimer nanosystems for constructing modular and effective contrast agents not only for MRI but also for MR/NIRF multimodality imaging. Such self-assembling dendrimer nanosystems can be applied to other multimodality imaging as well as to theranostics. Notably, multimodality imaging combines complementary information from

different imaging systems, thereby compensating for each of their weaknesses to provide more complete imaging data for precision medicine. The current study offers a promising nanotechnology platform based on modular and self-assembling dendrimer material for the creation of multimodality imaging agents for biomedical applications.

## 4. Experimental Section

*In Vivo Imaging Study:* All experimental procedures on animals were approved by the Animal Ethics Committee of Marseille Number 14 (N°: 2 019 042 518 563 696, 2 019 040 115 419 686). All mice were housed in specific pathogen-free conditions according to current European regulations. Female and male NMRI-Foxn1nu/Foxn1nu mice (nude mice) were provided by Janvier Laboratories. Mice were housed in environmentally-enriched cages placed in a temperature- and hygrometry-controlled room with daily monitoring, and were fed ad libitum with free access to water. A full description of the materials and methods as well as all experimental details is provided in the Supporting Information.

*In Vivo Toxicity Evaluation:* All procedures were approved by the Institutional Animal Care and Use Committee of China Pharmaceutical University and were performed in accordance with their guidelines and policies. The approval numbers were “2021-11-020” and “23-10-009”. Male CD-1 mice (6-week-old) were purchased from Sino-British SIPPR/BK Lab Animal Ltd (Shanghai, China). All mice involved in this work were kept at the Animal Center of China Pharmaceutical University Laboratory and received the required animal care and monitoring. A full description of the materials and methods as well as all experimental details is provided in the Supporting Information.

## Supporting Information

Supporting Information is available from the Wiley Online Library or from the author.

## Acknowledgements

This work was supported by the Ligue Nationale Contre le Cancer (EL2016, EL2021 LNCCLiP, LP; doctoral fellowship grant, ZL), China Scholarship Council (LD), the French National Research Agency under the framework of the ERA-NET EURONANOMED European Research project “NAN-4-TUM” (LP), the EU H2020 Research and Innovation program NMBP “SAFE-N-MEDTECH” (2019-2023) (grant agreement No. 814607, LP, TR), Fondation Recherche Médicale (YJ) and National Key Research & Development Program of China for International S&T Cooperation Projects (2018YFE0117800) (XL). The relaxometric and preclinical MRI studies were performed at CRMBM, which is a member of France Life Imaging (grant ANR-11-INBS-0006 from the French “Investissements d’Avenir” program).

## Conflict of Interest

The authors declare no conflict of interest.

and **DiR/Gd-1@** at a low dose (**DiR/Gd-1@-L**, 0.025 mmol Gd  $kg^{-1}$ , 67  $\mu g$  DiR/kg; lower panel) at different time points after injection. Red dashed circles indicate the tumor location, and yellow circles indicate the thigh muscle region used for signal normalization. F) Signal intensity ratio of tumor to adjacent muscles obtained from MRI data. Data denote mean  $\pm$  SD ( $n = 3$ ). The statistical significance was calculated by two-way ANOVA with Tukey’s multiple comparison test.  $^{**}P < 0.01$ ,  $^{***}P < 0.001$ ,  $^{****}P < 0.0001$  versus Gd-DOTA 0.5 h group;  $^{\#}P < 0.01$ ,  $^{\#\#\#}P < 0.0001$  versus **DiR/Gd-1@-L** Ctrl group;  $^{\&}P < 0.05$ ,  $^{\&\&}P < 0.001$  versus **DiR/Gd-1@-UL** Ctrl group;  $^{\Delta}P < 0.05$  versus **DiR/Gd-1@-UL** 48 h group;  $^{||}P < 0.01$  versus **DiR/Gd-1@-L** 48 h group. G) NIRF images after in vivo MRI at 48 h post-injection. H) Fluorescence intensity ratio of tumor to adjacent muscle obtained from NIRF imaging data. Red circles indicate the tumor locations. Data denote mean  $\pm$  SD ( $n = 3$ ). The statistical significance was calculated by a two-tailed Student’s  $t$ -test for comparison between the two groups.  $^{**}P < 0.01$ .

## Author Contributions

L.P. conceived and coordinated the project. L.D., Z.L., A.Y.T.H., and T.R. synthesized the agents. L.D., Z.L., S.G., and T.A.P.B. performed the characterization. J.I. provided the animal model. L.D., Y.J., and B.L. performed the animal experiments. L.D., B.L., and C.G. assessed toxicity. T.A.P.B., A.V., L.D., and Y.J. performed in vivo imaging experiments. L.D., Z.L., A.Y.T.H., C.-L.K., X.L., T.A.P.B., A.V., M.B., and L.P. analyzed the data. L.D., T.A.P.B., A.V., X.L., M.B., and L.P. wrote the paper. All authors proofread the manuscript.

## Data Availability Statement

The data that support the findings of this study are available from the corresponding author upon reasonable request.

## Keywords

dendrimers, MRI (magnetic resonance imaging), Near-infrared fluorescence (NIRF) imaging, pancreatic cancer, self-assembling

Received: August 15, 2023

Revised: November 26, 2023

Published online:

- [1] M. L. James, S. S. Gambhir, *Physiol. Rev.* **2012**, *92*, 897.
- [2] Editorial, Believing in seeing, *Nat. Mater.* **2014**, *13*, 99.
- [3] B. R. Smith, S. S. Gambhir, *Chem. Rev.* **2017**, *117*, 901.
- [4] H. Chen, W. Zhang, G. Zhu, J. Xie, X. Chen, *Nat. Rev. Mater.* **2017**, *2*, 17024.
- [5] Y. Matsumura, H. Maeda, *Cancer Res.* **1986**, *46*, 6387.
- [6] L. E. Gerlowski, R. K. Jain, *Microvasc. Res.* **1986**, *31*, 288.
- [7] H. Maeda, J. Wu, T. Sawa, Y. Matsumura, K. Hori, *J. Controlled Release* **2000**, *65*, 271.
- [8] H. Maeda, *Adv. Drug Delivery Rev.* **2015**, *91*, 3.
- [9] Y. Shi, R. van der Meel, X. Chen, T. Lammers, *Theranostics* **2020**, *10*, 7921.
- [10] R. Sun, J. Xiang, Q. Zhou, Y. Piao, J. Tang, S. Shao, Z. Zhou, Y. H. Bae, Y. Shen, *Adv. Drug Delivery Rev.* **2022**, *191*, 114614.
- [11] G. H. Petersen, S. K. Alzghari, W. Chee, S. S. Sankari, N. M. La-Beck, *J. Controlled Release* **2016**, *232*, 255.
- [12] A. Nel, E. Ruoslahti, H. Meng, *ACS Nano* **2017**, *11*, 9567.
- [13] I. de Lázaro, D. J. Mooney, *Nat. Mater.* **2020**, *19*, 486.
- [14] Y. Matsumoto, J. W. Nichols, K. Toh, T. Nomoto, H. Cabral, Y. Miura, R. J. Christie, N. Yamada, T. Ogura, M. R. Kano, Y. Matsumura, N. Nishiyama, T. Yamasoba, Y. H. Bae, K. Kataoka, *Nat. Nanotechnol.* **2016**, *11*, 533.
- [15] J. K. Tee, L. X. Yip, E. S. Tan, S. Santitewagun, A. Prasath, P. C. Ke, H. K. Ho, D. T. Leong, *Chem. Soc. Rev.* **2019**, *48*, 5381.
- [16] S. Sindhvani, A. M. Syed, J. Ngai, B. R. Kingston, L. Maiorino, J. Rothschild, P. MacMillan, Y. Zhang, N. U. Rajesh, T. Hoang, J. L. Y. Wu, S. Wilhelm, A. Zilman, S. Gadde, A. Sulaiman, B. Ouyang, Z. Lin, L. Wang, M. Egeblad, W. C. W. Chan, *Nat. Mater.* **2020**, *19*, 566.
- [17] S. Chen, Y. Zhong, W. Fan, J. Xiang, G. Wang, Q. Zhou, J. Wang, Y. Geng, R. Sun, Z. Zhang, Y. Piao, J. Wang, J. Zhuo, H. Cong, H. Jiang, J. Ling, Z. Li, D. Yang, X. Yao, X. Xu, Z. Zhou, J. Tang, Y. Shen, *Nat. Biomed. Eng.* **2021**, *5*, 1019.
- [18] X. Wu, T. Tang, Y. Wei, K. A. Cummins, D. K. Wood, H.-B. Pang, *Adv. Sci.* **2022**, *9*, 2102441.
- [19] Y. Jiang, Z. Lyu, B. Rahaly, J. Liu, T. Roussel, L. Ding, J. Tang, A. Kosta, S. Giorgio, R. Tomasini, X.-J. Liang, N. Dusetti, J. Iovanna, L. Peng, *Proc. Natl. Acad. Sci. U. S. A.* **2023**, *120*, e2215308120.
- [20] J.-M. Lehn, *Science* **2002**, *295*, 2400.
- [21] A. C. Mendes, E. T. Baran, R. L. Reis, H. S. Azevedo, *Wiley Interdiscip. Rev.: Nanomed. Nanobiotechnol.* **2013**, *5*, 582.
- [22] P. Garrigue, J. Tang, L. Ding, A. Bouhellel, A. Tintaru, E. Laurini, Y. Huang, Z. Lyu, M. Zhang, S. Fernandez, L. Balasse, W. Lan, E. Mas, D. Marson, Y. Weng, X. Liu, S. Giorgio, J. Iovanna, S. Pricl, B. Guillet, L. Peng, *Proc. Natl. Acad. Sci. U. S. A.* **2018**, *115*, 11454.
- [23] L. Ding, Z. Lyu, A. Tintaru, E. Laurini, D. Marson, B. Louis, A. Bouhellel, L. Balasse, S. Fernandez, P. Garrigue, E. Mas, S. Giorgio, S. Pricl, B. Guillet, L. Peng, *Chem. Commun.* **2020**, *56*, 301.
- [24] L. Ding, Z. Lyu, B. Louis, A. Tintaru, E. Laurini, D. Marson, M. Zhang, W. Shao, Y. Jiang, A. Bouhellel, L. Balasse, P. Garrigue, E. Mas, S. Giorgio, J. Iovanna, Y. Huang, S. Pricl, B. Guillet, L. Peng, *Small* **2020**, *16*, 2003290.
- [25] J. Chen, D. Zhu, X. Liu, L. Peng, *Acc. Mater. Res.* **2022**, *3*, 484.
- [26] Z. Lyu, L. Ding, A. Tintaru, L. Peng, *Acc. Chem. Res.* **2020**, *53*, 2936.
- [27] M. G. Harisinghani, A. O'Shea, R. Weissleder, *Sci. Transl. Med.* **2019**, *11*, eaba2591.
- [28] E. Terreno, D. D. Castelli, A. Viale, S. Aime, *Chem. Rev.* **2010**, *110*, 3019.
- [29] J. Wahsner, E. M. Gale, A. Rodríguez-Rodríguez, P. Caravan, *Chem. Rev.* **2019**, *119*, 957.
- [30] A. J. L. Villaraza, A. Bumb, M. W. M. Brechbiel, *Chem. Rev.* **2010**, *110*, 2921.
- [31] K. Wang, Y. Du, Z. Zhang, K. He, Z. Cheng, L. Yin, D. Dong, C. Li, W. Li, Z. Hu, C. Zhang, H. Hui, C. Chi, J. Tian, *Nat. Rev. Bioeng.* **2023**, *1*, 161.
- [32] G. Hong, A. L. Antaris, H. Dai, *Nat. Biomed. Eng.* **2017**, *1*, 0010.
- [33] Z. Hu, C. Fang, B. Li, Z. Zhang, C. Cao, M. Cai, S. Su, X. Sun, X. Shi, C. Li, T. Zhou, Y. Zhang, C. Chi, P. He, X. Xia, Y. Chen, S. S. Gambhir, Z. Cheng, J. Tian, *Nat. Biomed. Eng.* **2020**, *4*, 259.
- [34] C. Wang, W. Fan, Z. Zhang, Y. Wen, L. Xiong, X. Chen, *Adv. Mater.* **2019**, *31*, 1904329.
- [35] P. Caravan, J. J. Ellison, T. J. McMurry, R. B. Lauffer, *Chem. Rev.* **1999**, *99*, 2293.
- [36] J. Kleeff, M. Korc, M. Apte, C. La Vecchia, C. D. Johnson, A. V. Biankin, R. E. Neale, M. Tempero, D. A. Tuveson, R. H. Hruban, J. P. Neoptolemos, *Nat. Rev. Dis. Primers* **2016**, *2*, 16022.
- [37] C. J. Halbrook, C. A. Lyssiotis, M. Pasca di Magliano, A. Maitra, *Cell* **2023**, *186*, 1729.
- [38] J. D. Mizrahi, R. Surana, J. W. Valle, R. T. Shroff, *Lancet* **2020**, *395*, 2008.
- [39] S. P. Pereira, L. Oldfield, A. Ney, P. A. Hart, M. G. Keane, S. J. Pandol, D. Li, W. Greenhalf, C. Y. Jeon, E. J. Koay, C. V. Almario, C. Halloran, A. M. Lennon, E. Costello, *Lancet Gastroenterol. Hepatol.* **2020**, *5*, 698.
- [40] V. P. Chauhan, R. K. Jain, *Nat. Mater.* **2013**, *12*, 958.
- [41] H. Cabral, Y. Matsumoto, K. Mizuno, Q. Chen, M. Murakami, M. Kimura, Y. Terada, M. R. Kano, K. Miyazono, M. Uesaka, N. Nishiyama, K. Kataoka, *Nat. Nanotechnol.* **2011**, *6*, 815.
- [42] V. P. Chauhan, T. Stylianopoulos, J. D. Martin, Z. Popović, O. Chen, W. S. Kamoun, M. G. Bawendi, D. Fukumura, R. K. Jain, *Nat. Nanotechnol.* **2012**, *7*, 383.
- [43] Y. Shen, F. L. Goerner, C. Snyder, J. N. Morelli, D. Hao, D. Hu, X. Li, V. M. Runge, *Invest. Radiol.* **2015**, *50*, 330.
- [44] D. Levine, R. J. McDonald, H. Y. Kressel, *JAMA, J. Am. Med. Assoc.* **2018**, *320*, 1853.
- [45] J. Davies, P. Siebenhandl-Wolff, F. Tranquart, P. Jones, P. Evans, *Arch. Toxicol.* **2022**, *96*, 403.
- [46] J. Liu, C. Chen, T. Wei, O. Gayet, C. Loncle, L. Borge, N. Dusetti, X. Ma, D. Marson, E. Laurini, S. Pricl, Z. Gu, J. Iovanna, L. Peng, X.-J. Liang, *Exploration* **2021**, *1*, 21.
- [47] C. Commisso, *Philos. Trans. R. Soc., B* **2019**, *374*, 20180153.
- [48] W. Yao, J. L. Rose, W. Wang, S. Seth, H. Jiang, A. Taguchi, J. Liu, L. Yan, A. Kapoor, P. Hou, Z. Chen, Q. Wang, L. Nezi, Z. Xu, J. Yao, B.

- Hu, P. F. Pettazzoni, I. L. Ho, N. Feng, V. Ramamoorthy, S. Jiang, P. Deng, G. J. Ma, P. Den, Z. Tan, S. X. Zhang, H. Wang, Y. A. Wang, A. K. Deem, J. B. Fleming, et al., *Nature* **2019**, 568, 410.
- [49] T. Wei, C. Chen, J. Liu, C. Liu, P. Posocco, X. Liu, Q. Cheng, S. Huo, Z. Liang, M. Fermeglia, S. Pricl, X.-J. Liang, P. Rocchi, L. Peng, *Proc. Natl. Acad. Sci. U. S. A.* **2015**, 112, 2978.
- [50] M. Allard, D. Doucet, P. Kien, B. Bonnemain, J. M. Caillé, *Invest. Radiol.* **1988**, 23, S271.
- [51] E. C. Wiener, M. W. Brechbiel, H. Brothers, R. L. Magin, O. A. Gansow, D. A. Tomalia, P. C. Lauterbur, *Magn. Reson. Med.* **1994**, 31, 1.
- [52] K. Luo, G. Liu, X. Zhang, W. She, B. He, Y. Nie, L. Li, Y. Wu, Z. Zhang, Q. Gong, F. Gao, B. Song, H. Ai, Z. Gu, *Macromol. Biosci.* **2009**, 9, 1227.
- [53] H. Li, J. Sun, H. Zhu, H. Wu, H. Zhang, Z. Gu, K. Luo, *Wiley Interdiscip. Rev.: Nanomed. Nanobiotechnol.* **2021**, 13, e1670